

The CO-to-H₂ Conversion Factor in the Central Molecular Zone of the Milky Way using CO isotopologues

Mikito Kohno^{1,2*} and Yoshiaki Sofue³

¹Astronomy Section, Nagoya City Science Museum, 2-17-1 Sakae, Naka-ku, Nagoya, Aichi 460-0008, Japan

²Department of Physics, Graduate School of Science, Nagoya University, Furo-cho, Chikusa-ku, Nagoya, Aichi 464-8602, Japan

³Institute of Astronomy, The University of Tokyo, 2-21-1 Osawa, Mitaka, Tokyo 181-0015, Japan

*E-mail: kohno@nagoya-p.jp, mikito.kohno@gmail.com

Received 2024 February 2; Accepted 2024 April 4

Abstract

We performed correlation analyses between the ¹²CO and ¹³CO $J=1-0$ line intensities in order to derive the variability of the CO-to-H₂ conversion factor ($X_{\text{CO,iso}}$) in the central molecular zone (CMZ) of our Galaxy. New high-resolution $X_{\text{CO,iso}}$ maps at a resolution of $\sim 30''$ and the longitude-velocity diagram (LVD) at resolution $\sim 30'' \times 2 \text{ km s}^{-1}$ are presented using the ¹²CO and ¹³CO archival survey data obtained by the Nobeyama 45 m telescope. We revealed the variation of $X_{\text{CO,iso}}$ in the CMZ within the range of $X_{\text{CO,iso}} \sim (0.2 - 1.3) \times 10^{20} \text{ cm}^{-2} (\text{K km s}^{-1})^{-1}$, if we assume the normalization value of $0.59 \times 10^{20} \text{ cm}^{-2} (\text{K km s}^{-1})^{-1}$. The mean value is obtained as $X_{\text{CO,iso}} = (0.48 \pm 0.15) \times 10^{20} \text{ cm}^{-2} (\text{K km s}^{-1})^{-1}$ in the CMZ of our Galaxy.

Key words: Galaxy: center — ISM: clouds — ISM: molecules — ISM: radio lines — ISM: general

1 Introduction

The Central Molecular Zone (hereafter CMZ) is the concentration of molecular gas within $\sim 300 \text{ pc}$ in the Galactic Center (GC; Morris & Serabyn 1996; Henshaw et al. 2023). The total molecular mass in the CMZ has been derived to be $\sim 2.3 \times 10^7 M_{\odot}$ assuming the CO-to-H₂ conversion factor of $X_{\text{CO}} = 0.51 \times 10^{20} \text{ cm}^{-2} (\text{K km s}^{-1})^{-1}$ (Sofue 2022), but it directly depends on the assumed value of X_{CO} , which is still uncertain in the GC (Dahmen et al. 1998). Hence, the mass, the most fundamental parameter of the GC, is still uncertain by a factor of ~ 2 to 4. The conversion factor is defined by

$$X_{\text{CO}} = \frac{N(\text{H}_2)_{12\text{X}}}{I_{12\text{CO}}} [\text{cm}^{-2} (\text{K km s}^{-1})^{-1}], \quad (1)$$

where $N(\text{H}_2)_{12\text{X}}$ is the H₂ column density and $I_{12\text{CO}}$ is the integrated intensity of the ¹²CO $J=1-0$ line. The standard value of the X_{CO} factor is $2 \times 10^{20} \text{ cm}^{-2} (\text{K km s}^{-1})^{-1}$ with the uncertainty of $\pm 30\%$ in the Galactic disk (Bolatto et al. 2013).

In the GC, X_{CO} is suggested to be significantly smaller than the local value due to the higher metallicity (Arimoto et al. 1996), decreasing by a factor of $\sim 3-10$ (Bolatto et al. 2013). Lower X_{CO} factors have been also pointed out comparison of the CO luminosity with the γ ray brightness (Blitz et al. 1985; Strong et al. 2004), analysis of the infrared dust emission (Sodroski et al. 1995; Schultheis et al. 2014), and Virial mass (Oka et al. 1998a).

Recently, Sofue & Kohno (2020, hereafter: Paper I) and Kohno & Sofue (2024, hereafter: Paper II) revealed

the variability of the X_{CO} factor in the Galactic giant molecular clouds (GMC). These papers present the high-resolution ($\sim 15''$) X_{CO} maps using CO isotopologues obtained by the FUGIN CO survey data (Umemoto et al. 2017; Torii et al. 2019).

In this paper, we aim first at deriving the X_{CO} variability in the GC at higher accuracy and at presenting detailed distributions of X_{CO} in longitude-latitude (l, b) and longitude-velocity (l, V_{LSR}) planes at high angular and velocity resolutions using the CO-line data from the Nobeyama 45-m radio telescope.

2 Data

We used the high-resolution CO $J=1-0$ archival data of the Galactic center obtained by the Nobeyama 45 m telescope (Tokuyama et al. 2019)¹. The ^{12}CO and ^{13}CO $J=1-0$ data were obtained by the multi-beam receiver of BEARS (25-BEam Array Receiver System: Sunada et al. 2000; Yamaguchi et al. 2000) and FOREST (FOur beam REceiver System on the 45-m Telescope Minamidani et al. 2016; Nakajima et al. 2019) installed in the Nobeyama 45 m telescope. The full width half-maximum beam size is approximately $15''$ at 115 GHz and 110 GHz. The intensity is calibrated to the radiation temperature (T_R^* : Kutner & Ulich 1981) comparing with the previous CO survey data observed by the Nobeyama 45 m telescope (Oka et al. 1998b). Here, T_R^* corresponds to the brightness temperature T_B of a spatially resolved (extended) source. The final data used in this paper has a grid spacing with $(l, b, v) = (7''.5, 7''.5, 2 \text{ km s}^{-1})$. We smoothed the archival data to $\sim 30''$ using the kernel Gaussian function to improve the signal-to-noise ratio. The root-mean-square (r.m.s) noise levels of the final cube data are $\sim 0.4 \text{ K}$ and $\sim 0.1 \text{ K}$ for ^{12}CO and ^{13}CO $J=1-0$, respectively.

3 Methods

In this study, we calculated the column densities of molecular hydrogen using the integrated intensity of ^{12}CO and ^{13}CO $J=1-0$. The H_2 column density is taken from the ^{12}CO integrated intensity by assuming the X_{CO} factor from the equation (1). We used the conversion factor of $X_{\text{CO}} = 0.59 \times 10^{20} \text{ cm}^{-2} (\text{K km s}^{-1})^{-1}$ (Arimoto et al. 1996) currently obtained for the Galactic Center region as the normalization value in this article. This value has been obtained by extrapolating the X_{CO} values determined in the disc to the GC by assuming a scale radius of the Galactic disc, $r_e = 6.2 \text{ kpc}$, and the distance of the

GC from the Sun, $R_0 = 8.0 \text{ kpc}$ (Reid et al. 2019; VERA Collaboration et al. 2020).

Independent of the conversion factor, we derived the H_2 column density in the CMZ by the local thermal equilibrium (LTE) method described in Paper I, II, and Pineda et al. (2008). The brightness temperature (T_B) of the CO line intensity with the excitation temperature (T_{ex}) and the optical depth (τ) is given by

$$T_B = T_0 \left(\frac{1}{e^{T_0/T_{\text{ex}}} - 1} - \frac{1}{e^{T_0/T_{\text{bg}}} - 1} \right) (1 - e^{-\tau}) \text{ [K]}, \quad (2)$$

where $T_{\text{bg}} = 2.73 \text{ K}$ is the temperature of the cosmic-microwave background radiation. $T_0 = h\nu/k$ is the Planck temperature with h , ν , and k being the Planck constant, rest frequency, and Boltzman constant, respectively.

If we assume that the ^{12}CO line is optically thick, the excitation temperature is given by

$$T_{\text{ex}} = T_0^{115} / \ln \left(1 + \frac{T_0^{115}}{T_B(^{12}\text{CO})_{\text{max}} + 0.836} \right) \text{ [K]}, \quad (3)$$

where $T_B(^{12}\text{CO})_{\text{max}}$ and $T_0^{115} = 5.53 \text{ K}$ correspond to the ^{12}CO peak brightness temperature and the Planck temperature at the rest frequency of ^{12}CO $J=1-0$, respectively. In the longitude-latitude ($l-b$) and longitude-velocity ($l-v$) space, T_{ex} at each pixel is calculated using the peak value along the velocity-axis and latitude-axis, respectively. We assume that T_{ex} is equal in the ^{12}CO and ^{13}CO line emissions, and express the optical depth as

$$\tau(^{13}\text{CO}) = -\ln \left(1 - \frac{T_B(^{13}\text{CO})_{\text{max}}/T_0^{110}}{(e^{T_0^{110}/T_{\text{ex}}} - 1)^{-1} - 0.168} \right), \quad (4)$$

where $T_B(^{13}\text{CO})_{\text{max}}$ and $T_0^{110} = 5.29 \text{ K}$ represent the ^{13}CO peak brightness temperature and the Planck temperature at the rest frequency of ^{13}CO $J=1-0$, respectively. The ^{13}CO column density is given by

$$N_{^{13}\text{CO}} = 3.0 \times 10^{14} \frac{\tau}{1 - e^{-\tau}} \frac{I_{^{13}\text{CO}}}{1 - e^{-T_0^{110}/T_{\text{ex}}}} \text{ [cm}^{-2}\text{]}, \quad (5)$$

where $I_{^{13}\text{CO}}$ is the ^{13}CO integrated intensity. Then, we convert $N_{^{13}\text{CO}}$ to the H_2 column density using the abundance ratio of H_2 to ^{13}CO molecules given by

$$N(\text{H}_2)_{13\text{L}} = Y_{\text{GC}^{13}\text{CO}} N_{^{13}\text{CO}} \text{ [cm}^{-2}\text{]}. \quad (6)$$

Here, $Y_{\text{GC}^{13}\text{CO}}$ is adopted as $\sim 1 \times 10^6$ in Sagittarius B2 (Lis & Goldsmith 1989).

4 Results

4.1 CO spatial and velocity distributions in the CMZ

Figure 1 (a) shows the integrated intensity map of ^{12}CO $J=1-0$. The integrated velocity range is from -219 km s^{-1} to $+221 \text{ km s}^{-1}$. ^{12}CO has a peak at the GMC complex of Sagittarius B2 (Sgr B2), Sagittarius C (Sgr C), and $l =$

¹ <https://www.nro.nao.ac.jp/~nro45mrt/html/results/data.html>

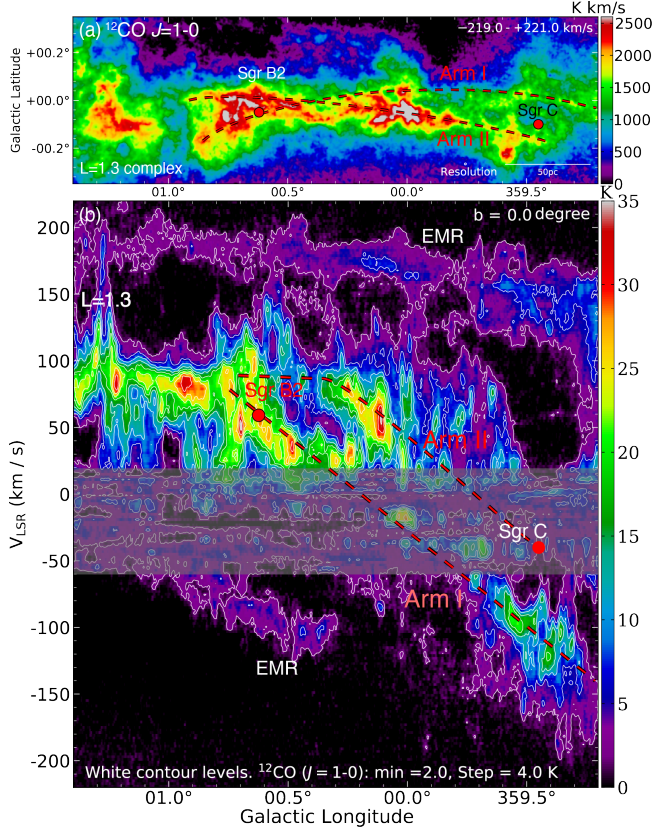


Fig. 1. (a) The integrated intensity map of $^{12}\text{CO } J=1-0$ obtained by the Nobeyama 45 m telescope (Tokuyama et al. 2019). The integrated velocity range is from -219 km s^{-1} to 221 km s^{-1} . (b) The longitude-velocity diagram of ^{12}CO at $b = 0^\circ$. Arm I and Arm II are pointed in red dashed lines, that is spiral arms around Sgr A (Sofue 1995a). The lowest white contour level and intervals of the panel are 2.0 and 4.0 K. The shadow area from -60 to $+20 \text{ km s}^{-1}$ is contaminated by the foreground spiral arms (e.g., Oka et al. 2001; Sofue 2006; Reid et al. 2016). The red points show the positions of Sgr B2 and Sgr C.

$1^\circ.3$ complex. Molecular gas shows $\sim 50 \text{ pc}$ distributions of each GMC complex. Figure 1(b) shows the longitude-velocity diagram (LVD) of $^{12}\text{CO } J=1-0$ cutting at $b = 0^\circ$. The red dashed lines show Arm I and Arm II of the spiral arms around Sgr A (Sofue 1995a). The CMZ is distributed from -200 km s^{-1} to $+200 \text{ km s}^{-1}$ on the velocity space. We can also find the Expanding Molecular Ring (EMR) with the non-circular gas motion around the GC (Kaifu et al. 1972; Kaifu et al. 1974; Scoville 1972; Sofue 1995b). The shadowed area at the velocity range from -60 km s^{-1} to $+20 \text{ km s}^{-1}$ is contaminated by the GC's foreground spiral arms (Oka et al. 1998b; Sofue 2006).

4.2 $X_{\text{CO,iso}}$ maps

Figure 2 shows the scatter plots between $N(\text{H}_2)_{13\text{L}}$ and $N(\text{H}_2)_{12\text{X}}$ in the CMZ. Black dashed line indicates the linear relation of $N(\text{H}_2)_{12\text{X}} = N(\text{H}_2)_{13\text{L}}$. $N(\text{H}_2)_{12\text{X}}$ shows

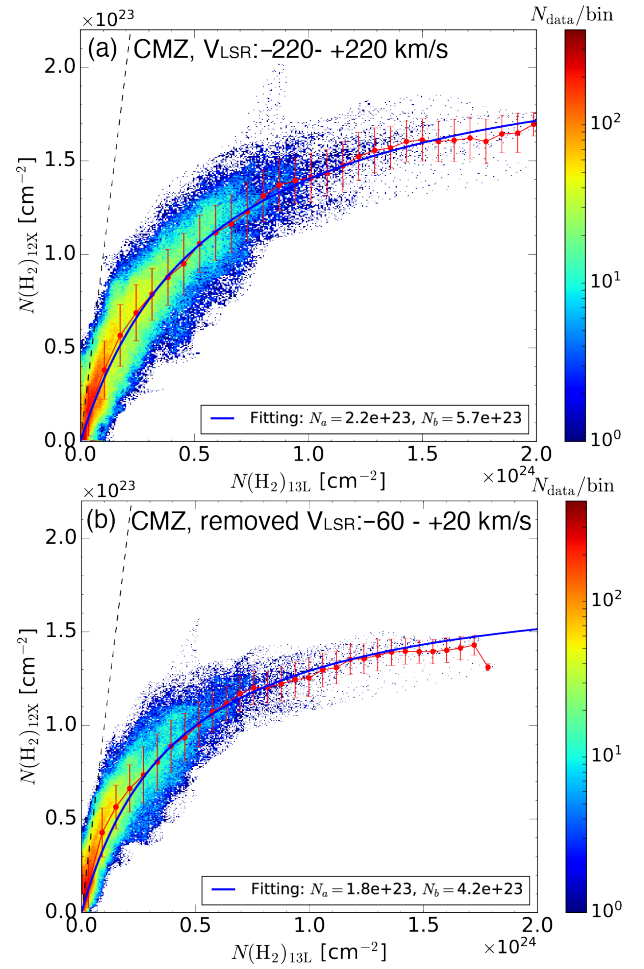


Fig. 2. (a) Scatter plots between $N(\text{H}_2)_{13\text{L}}$ and $N(\text{H}_2)_{12\text{X}}$ of the CMZ. Red points show the averaged values of each bin, and the error bars are standard deviations of $N(\text{H}_2)_{12\text{X}}$. Blue curves indicate the fitting results of scatter plots. The black dashed lines indicate the linear relation of $N(\text{H}_2)_{12\text{X}} = N(\text{H}_2)_{13\text{L}}$. (b) Same as (a), but for contaminated velocity range at $-60 \leq V_{\text{LSR}} < +20 \text{ km s}^{-1}$ are removed. The color bars show the number of data points in a bin ($N_{\text{data}}/\text{bin}$).

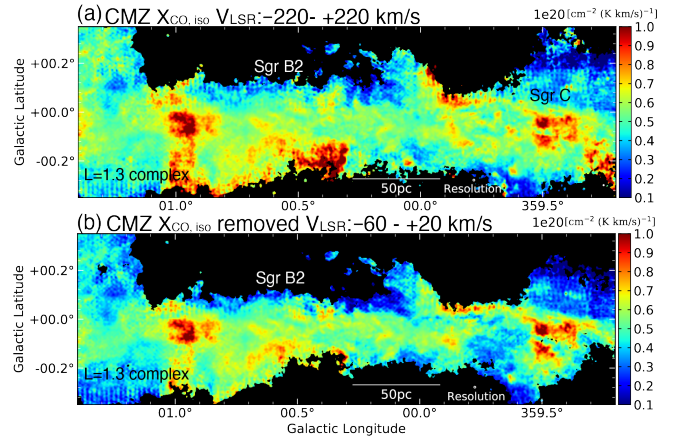


Fig. 3. (a) Spatial distributions of $X_{\text{CO,iso}}$ in the CMZ. The map is presented of $I_{12\text{CO}} > 500 \text{ K km s}^{-1}$. (b) Same, but contaminated velocity range at $-60 \leq V_{\text{LSR}} < +20 \text{ km s}^{-1}$ are removed.

Table 1. Fitting results and $\langle X_{\text{CO,iso}} \rangle$ taken from the correlation between $N(\text{H}_2)_{13\text{L}}$ and $N(\text{H}_2)_{12\text{X}}$.

Name	l	b	V_{LSR}	N_a	N_b	$\langle X_{\text{CO,iso}} \rangle$	C.C
	[deg]	[deg]	[km s $^{-1}$]	[10^{23} cm $^{-2}$]	[10^{23} cm $^{-2}$]	[10^{20} cm $^{-2}$ (K km s $^{-1}$) $^{-1}$]	
(1)	(2)	(3)	(4)	(5)	(6)	(7)	(8)
CMZ (all)	—	—	[−220, 220]	2.2	5.7	0.54 ± 0.16	0.89
CMZ ^[1]	—	—	[−220, −60] [20, 220]	1.8	4.2	0.48 ± 0.15	0.87
Sgr B2	0.62	−0.05	[20, 150]	1.9	4.7	0.54 ± 0.14	0.92
Sgr C	−0.55	−0.10	[−90, −30]	0.46	1.1	0.56 ± 0.16	0.87
$l=1.^\circ 3$	1.3	−0.1	[20, 150]	1.5	2.3	0.59 ± 0.11	0.92

[1] The velocity components from -60 km s $^{-1}$ to 20 km s $^{-1}$ were removed. Columns: (1) Region names, (2) Galactic longitude, (3) Galactic latitude, (4) Integrated velocity range, (5),(6) The fitting parameters of the non-linear relation. (7) The mean value of $X_{\text{CO,iso}}$ in the each region. (8) Correlation coefficient. The errors of mean value are adopted as the standard deviation in all pixels. $\langle X_{\text{CO,iso}} \rangle$ of the individual regions are derived by the data points of $I_{12\text{CO}} > 200$ K km s $^{-1}$.

saturation at high $N(\text{H}_2)_{13\text{L}}$, and the nonlinear relation. Then, we carried out the empirical curve fitting using the relation of

$$N(\text{H}_2)_{12\text{X}} = \frac{N_a N(\text{H}_2)_{13\text{L}}}{N(\text{H}_2)_{13\text{L}} + N_b} [\text{cm}^{-2}], \quad (7)$$

where N_a and N_b [both in H $_2$ cm $^{-2}$] are fitting parameters of the nonlinear relation having the same dimension as the column density. From the equation 1 and 7, we calculated the X_{CO} factor (hereafter $X_{\text{CO,iso}}$) of each pixel using the following relation of

$$X_{\text{CO,iso}} = \left(\frac{N_a N(\text{H}_2)_{13\text{L}}}{N(\text{H}_2)_{13\text{L}} + N_b} \right) / I_{12\text{CO}} [\text{cm}^{-2}(\text{K km s}^{-1})^{-1}]. \quad (8)$$

Figure 3(a) and 3(b) show the $X_{\text{CO,iso}}$ maps of the CMZ with the integrated velocity range from -220 to $+220$ km s $^{-1}$ and removed velocity range from -60 to $+20$ km s $^{-1}$, respectively. $X_{\text{CO,iso}}$ in the GMZ shows the variation of $(0.2 - 1.0) \times 10^{20}$ cm $^{-2}$ (K km s $^{-1}$) $^{-1}$. We obtained the mean value as $X_{\text{CO,iso}} = (0.54 \pm 0.16) \times 10^{20}$ and $X_{\text{CO,iso}} = (0.48 \pm 0.15) \times 10^{20}$ cm $^{-2}$ (K km s $^{-1}$) $^{-1}$ in Figure 3(a) and 3(b), respectively. The mean $X_{\text{CO,iso}}$ removed from the contaminated components is lower than all integrated velocity ranges. We also performed the curve fitting of the correlation between N_a and N_b of the individual regions in the CMZ. As a result, the mean $X_{\text{CO,iso}}$ is obtained in Sgr B2, Sgr C, and the $L = 1.^\circ 3$ complex. Table 1 presents the fitting parameters and $X_{\text{CO,iso}}$ of our analysis.

4.3 The $X_{\text{CO,iso}}$ longitude-velocity diagram

We made the $X_{\text{CO,iso}}$ LVD of the CMZ at the Galactic plane using the correlation of spectral column densities (SCD) obtained by the ^{12}CO and ^{13}CO intensity described as Paper I and Paper II. The $\text{SCD}_{12\text{X}}$ and $\text{SCD}_{13\text{L}}$ is given by

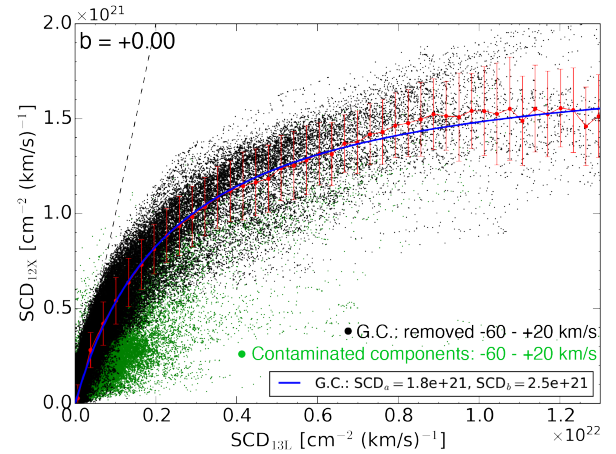


Fig. 4. Scatter plots between $\text{SCD}_{13\text{L}}$ and $\text{SCD}_{12\text{X}}$ on the longitude-velocity space at $b = 0.^\circ 0$. Black points show the -220 km s $^{-1} < V_{\text{LSR}} < -60$ km s $^{-1}$ and $+20$ km s $^{-1} < V_{\text{LSR}} < +220$ km s $^{-1}$ component. Green points present the -60 km s $^{-1} < V_{\text{LSR}} < +20$ km s $^{-1}$ component. Red points show the averaged values of each bin, and the error bars are standard deviations of $N(\text{H}_2)_{12\text{X}}$. The blue curve indicates the fitting result of the Galactic center components. The black dashed lines indicate the linear relation of $\text{SCD}_{12\text{X}} = \text{SCD}_{13\text{L}}$.

$$\begin{aligned} \text{SCD}_{12\text{X}} &= \frac{dN(\text{H}_2)_{12\text{X}}}{dv} \\ &= X_{\text{CO}} T_{\text{B}}(^{12}\text{CO}) [\text{cm}^{-2}(\text{km s}^{-1})^{-1}] \end{aligned} \quad (9)$$

and

$$\begin{aligned} \text{SCD}_{13\text{L}} &= \frac{dN(\text{H}_2)_{13\text{L}}}{dv} [\text{cm}^{-2}(\text{km s}^{-1})^{-1}] \\ &= 3.0 \times 10^{14} \frac{\tau}{1 - e^{-\tau}} \frac{Y_{13\text{CO}} T_{\text{B}}(^{13}\text{CO})}{1 - e^{-T_0^{110}/T_{\text{ex}}}}, \end{aligned} \quad (10)$$

respectively. $\text{SCD}_{12\text{X}}$ and $\text{SCD}_{13\text{L}}$ are the H $_2$ column densities at assuming a normalization value of $X_{\text{CO}} = 0.59 \times 10^{20}$ cm $^{-2}$ (K km s $^{-1}$) $^{-1}$ (Arimoto et al. 1996) and $Y_{\text{G}^{13}\text{CO}} = 1 \times 10^6$ (Lis & Goldsmith 1989), respectively. Figure 4 shows scatter plots between $\text{SCD}_{12\text{X}}$ and $\text{SCD}_{13\text{L}}$ in the longitude-velocity space at the Galactic

Table 2. $X_{\text{CO,iso}}$ on the LVD.

Name	V_{LSR} [km s ⁻¹]	$X_{\text{CO,iso}}$ [10 ²⁰ cm ⁻² (K km s ⁻¹) ⁻¹]
Arm I	—	~ 0.5 – 1.0
Arm II	—	~ 0.4 – 0.8
EMR	[150, 200] [-200, -100]	~ 0.2 – 1.3

plane ($b = 0.0^\circ$). Scatter plots on the longitude-velocity space at the different latitudes are presented in Figures 9a-14a of the Appendix. Green data points indicate from -60 km s^{-1} to $+20 \text{ km s}^{-1}$ contaminated by the foreground disk components. Black data points show the CMZ components with the removed from -60 km s^{-1} to $+20 \text{ km s}^{-1}$ components. The $\text{SCD}_{12\text{X}}$ saturation level of the GC is higher than contaminated components. We suggest that this result corresponds to the difference of the ^{12}CO and ^{13}CO ratio between the CMZ and the Galactic disk components reported in previous works (e.g., Figure 10 in Enokiya et al. 2023). Here, we performed the curve fitting to the GC components using the function of

$$\text{SCD}_{12\text{X}} = \frac{\text{SCD}_a \text{SCD}_{13\text{L}}}{\text{SCD}_{13\text{L}} + \text{SCD}_b} [\text{cm}^{-2}(\text{km s}^{-1})^{-1}], \quad (11)$$

where SCD_a and SCD_b correspond to the fitting parameters. The result of fitting parameters are obtained as $\text{SCD}_a = 1.8 \times 10^{21} \text{ cm}^{-2}(\text{km s}^{-1})^{-1}$ and $\text{SCD}_b = 2.5 \times 10^{21} \text{ cm}^{-2}(\text{km s}^{-1})^{-1}$. Then, $X_{\text{CO,iso}}$ in the LVD is given by

$$X_{\text{CO,iso}} = \left(\frac{\text{SCD}_a \text{SCD}_{13\text{L}}}{\text{SCD}_{13\text{L}} + \text{SCD}_b} \right) / T_{\text{B}}(^{12}\text{CO}) [\text{cm}^{-2}(\text{K km s}^{-1})^{-1}]. \quad (12)$$

Figure 5 shows the $X_{\text{CO,iso}}$ map on the LVD at $b = 0.0^\circ$. $X_{\text{CO,iso}}$ maps on the LVDs at the different latitudes are presented in Figures 9b-14b of the Appendix. The masked area presents the contaminated velocity range from the foreground disk components. This velocity range exists the CMZ gas and foreground disk gas in the same pixel of the data (see Figures 7 and 8 in the Appendix). In the optically thick ^{12}CO line, the emission from the CMZ is completely obscured and we only see the foreground gas. On the other hand, in the optically thin ^{13}CO line, we practically see the sum of the CMZ emission and foreground emission. In such a situation, the ^{12}CO and ^{13}CO lines trace totally different components. In this paper, we therefore focus on the variation of $X_{\text{CO,iso}}$ in the CMZ components, which are removed the contaminated velocity range on the LVD. $X_{\text{CO,iso}}$ has the variability of $X_{\text{CO,iso}} \sim (0.2 - 1.3) \times 10^{20} \text{ cm}^{-2}(\text{K km s}^{-1})^{-1}$ in the CMZ component on the LVD. We summarize the $X_{\text{CO,iso}}$ values on the LVD of Arm I, Arm II, and EMR in Table 2.

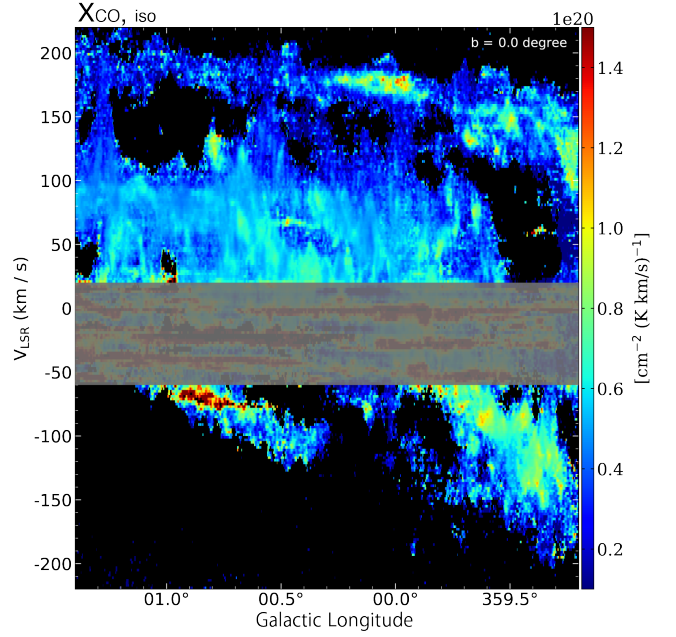


Fig. 5. Longitude-velocity distributions of $X_{\text{CO,iso}}$ in the CMZ at $b = 0.0^\circ$. The map is presented for $T_{\text{B}}(^{12}\text{CO}) > 1 \text{ K}$. The masked area shows the contaminated velocity range by the foreground disk components.

5 Discussion

We investigated the radial variation of $X_{\text{CO,iso}}$ based on the results of Paper II. Figure 6 shows the plot of $X_{\text{CO,iso}}$ as a function of the Galactocentric distance. $X_{\text{CO,iso}}$ of the GMCs in the Galactic disk were obtained by Paper II assuming the normalization value of $X_{\text{CO}} = 2 \times 10^{20} \text{ cm}^{-2}(\text{K km s}^{-1})^{-1}$ (Bolatto et al. 2013). In this paper, we assumed the normalization in the GC of $X_{\text{CO}} = 0.59 \times 10^{20} \text{ cm}^{-2}(\text{K km s}^{-1})^{-1}$ (Arimoto et al. 1996). Since the obtained value is proportional to this normalization factor if adopting a value of $2.0 \times 10^{20} \text{ cm}^{-2}(\text{K km s}^{-1})^{-1}$ of local molecular clouds, the whole results in our analysis must be multiplied by a factor of 3.39. The pink and yellow triangle in Figure 6 shows $X_{\text{CO,iso}}$ in the GC assuming the normalization X_{CO} of $2.0 \times 10^{20} \text{ cm}^{-2}(\text{K km s}^{-1})^{-1}$ and $0.59 \times 10^{20} \text{ cm}^{-2}(\text{K km s}^{-1})^{-1}$, respectively.

Finally, we compared $X_{\text{CO,iso}}$ in the CMZ with previous studies obtained by other methods to validate our assumption of the normalization value. The X_{CO} in the GC were taken from comparing the CO luminosity with the virial mass, gamma-ray brightness, extinction, infrared dust emission, and HI emission. Table 3 summarizes the Galactic Center X_{CO} values. Previous studies of X_{CO} in the GC are in the range of $(0.2 - 0.7) \times 10^{20} \text{ cm}^{-2}(\text{K km s}^{-1})^{-1}$, which is lower than the standard value of $2 \times 10^{20} \text{ cm}^{-2}(\text{K km s}^{-1})^{-1}$ in the Milky Way disk (Bolatto et al. 2013). Our results us-

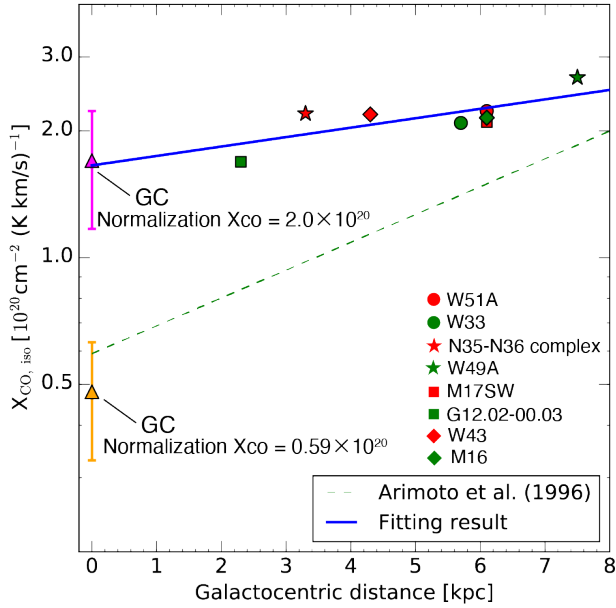


Fig. 6. Radial gradient of $X_{\text{CO,iso}}$ from the distance of the GC. The pink and yellow triangle shows $X_{\text{CO,iso}}$ in the GC assuming the normalization X_{CO} of $2.0 \times 10^{20} \text{ cm}^{-2} (\text{K km s}^{-1})^{-1}$ and $0.59 \times 10^{20} \text{ cm}^{-2} (\text{K km s}^{-1})^{-1}$, respectively. The vertical error bars of the GC indicate the standard deviation in the $X_{\text{CO,iso}}$ map. Other symbols present the individual GMCs of W51A, W33, N35-N36 complex, W49A, M17SW, G12.02-00.03, W43, and M16 obtained by Paper II. The blue line shows the fitting result to individual GMCs and GC assuming the normalization $X_{\text{CO}} = 2 \times 10^{20} \text{ cm}^{-2} (\text{K km s}^{-1})^{-1}$ by an exponential function. The green dashed line indicates the relation from Arimoto et al. (1996).

Table 3. Comparison with the previous studies of the X_{CO} factor in the Galactic Center region.

Method	X_{CO} [$10^{20} \text{ cm}^{-2} (\text{K km s}^{-1})^{-1}$]	References
Isotopologues	0.2–1.3 [†]	This study
	0.7–4.4*	This study
Virial	0.24	[1]
Gamma-rays	0.3–0.6	[2]
Extinction	0.3–0.6	[3]
Dust	0.2–0.7	[4]
Dust and HI	0.7 ± 0.1	[5]

We assumed the normalization X_{CO} value of [†] $0.59 \times 10^{20} \text{ cm}^{-2} (\text{K km s}^{-1})^{-1}$ and * $2.0 \times 10^{20} \text{ cm}^{-2} (\text{K km s}^{-1})^{-1}$. References [1] Oka et al. (1998a), [2] Ackermann et al. (2012) [3] Schultheis et al. (2014), [4] Sodroski et al. (1995), [5] Torii et al. (2010)

ing CO isotopologues assuming the normalization value of $X_{\text{CO}} = 0.59 \times 10^{20} \text{ cm}^{-2} (\text{K km s}^{-1})^{-1}$ shows the variation of $X_{\text{CO,iso}} \sim (0.2 - 1.3) \times 10^{20} \text{ cm}^{-2} (\text{K km s}^{-1})^{-1}$ in the GC, and its value is consistent with these previous works. These points show our assumption of the normalization X_{CO} of $0.59 \times 10^{20} \text{ cm}^{-2} (\text{K km s}^{-1})^{-1}$ based on Arimoto et al. (1996) is valid in this paper, whereas the fitting result shown in the blue line is consistent with the pink triangle obtained by the normalization value of $2 \times 10^{20} \text{ cm}^{-2} (\text{K km s}^{-1})^{-1}$. This inconsistency might be explained by the gradient between $X_{\text{CO,iso}}$ in the CMZ and the Galactic disk component is a discontinuous function of the Galactocentric distance. The absolute value of $X_{\text{CO,iso}}$ is influenced by the initially-assumed X_{CO} , while the relative variability of $X_{\text{CO,iso}}$ is independent of the normalization value. We point out that our assumption does not change the difference of $X_{\text{CO,iso}}$ on the longitude-latitude and longitude-velocity space.

6 Summary

The conclusions of this paper are summarized as follows:

1. We investigated the correlation between the ^{12}CO and ^{13}CO $J=1-0$ integrated intensities and the brightness temperatures in the central molecular zone of our Galaxy using the archival CO survey data obtained by the Nobeyama 45 m telescope. The non-linear relation is revealed between them.
2. We performed the curve fitting of the non-linear relation between the ^{12}CO and ^{13}CO $J=1-0$ intensities to derive the variability of the CO-to- H_2 conversion factor ($X_{\text{CO,iso}}$) in the CMZ.
3. The high-resolution $X_{\text{CO,iso}}$ maps ($\sim 30''$) and the longitude-velocity diagram are presented. The $X_{\text{CO,iso}}$ in the Galactic center region shows the variability of $X_{\text{CO,iso}} \sim (0.2 - 1.3) \times 10^{20} \text{ cm}^{-2} (\text{K km s}^{-1})^{-1}$ if we assume the normalization value of $X_{\text{CO}} = 0.59 \times 10^{20} \text{ cm}^{-2} (\text{K km s}^{-1})^{-1}$.
4. We obtained $X_{\text{CO,iso}} = (0.48 \pm 0.15) \times 10^{20} \text{ cm}^{-2} (\text{K km s}^{-1})^{-1}$ as the mean value in the CMZ of our Galaxy.

Acknowledgements

We are grateful to the anonymous referee for his/her thoughtful comments. The Nobeyama 45-m radio telescope is operated by the Nobeyama Radio Observatory. We utilized the Python software package for astronomy (Astropy Collaboration et al. 2013). The authors are grateful to Prof. Tomoharu Oka and the radio astronomy group of Keio University for the archival GC survey data using

the Nobeyama 45-m telescope.

References

- Ackermann, M., Ajello, M., Atwood, W. B., et al. 2012, *ApJ*, 750, 3
- Arimoto, N., Sofue, Y., & Tsujimoto, T. 1996, *PASJ*, 48, 275
- Astropy Collaboration, Robitaille, T. P., Tollerud, E. J., et al. 2013, *A&A*, 558, A33
- Blitz, L., Bloemen, J. B. G. M., Hermsen, W., et al. 1985, *A&A*, 143, 267
- Bolatto, A. D., Wolfire, M., & Leroy, A. K. 2013, *ARA&A*, 51, 207
- Dahmen, G., Huttemeister, S., Wilson, T. L., et al. 1998, *A&A*, 331, 959
- Enokiya, R., Sano, H., Filipović, M. D., et al. 2023, *PASJ*, 75, 970
- Henshaw, J. D., Barnes, A. T., Battersby, C., et al. 2023, *Protostars and Planets VII*, 534, 83
- Kaifu, N., Kato, T., & Iguchi, T. 1972, *Nature Physical Science*, 238, 105
- Kaifu, N., Iguchi, T., & Kato, T. 1974, *PASJ*, 26, 117
- Kohno, M. & Sofue, Y. 2024, *MNRAS*, 527, 9290 (Paper II)
- Kutner, M. L. & Ulich, B. L. 1981, *ApJ*, 250, 341
- Lis, D. C. & Goldsmith, P. F. 1989, *ApJ*, 337, 704
- Minamidani, T., Nishimura, A., Miyamoto, Y., et al. 2016, *Proc. SPIE*, 99141Z
- Morris, M. & Serabyn, E. 1996, *ARA&A*, 34, 645
- Nakajima, T., Inoue, H., Fujii, Y., et al. 2019, *PASJ*, 71, S17
- Oka, T., Hasegawa, T., Hayashi, M., et al. 1998a, *ApJ*, 493, 730
- Oka, T., Hasegawa, T., Sato, F., et al. 1998b, *ApJS*, 118, 455
- Oka, T., Hasegawa, T., Sato, F., et al. 2001, *ApJ*, 562, 348
- Pineda, J. E., Caselli, P., & Goodman, A. A. 2008, *ApJ*, 679, 481
- Reid, M. J., Dame, T. M., Menten, K. M., et al. 2016, *ApJ*, 823, 77
- Reid, M. J., Menten, K. M., Brunthaler, A., et al. 2019, *ApJ*, 885, 131
- Schultheis, M., Chen, B. Q., Jiang, B. W., et al. 2014, *A&A*, 566, A120
- Scoville, N. Z. 1972, *ApJL*, 175, L127
- Sodroski, T. J., Odegard, N., Dwek, E., et al. 1995, *ApJ*, 452, 262
- Sofue, Y. & Kohno, M. 2020, *MNRAS*, 497, 1851 (Paper I)
- Sofue, Y. 1995a, *PASJ*, 47, 527
- Sofue, Y. 1995b, *PASJ*, 47, 551
- Sofue, Y. 2006, *PASJ*, 58, 335
- Sofue, Y. 2022, *MNRAS*, 516, 907
- Strong, A. W., Moskalenko, I. V., Reimer, O., et al. 2004, *A&A*, 422, L47
- Sunada, K., Yamaguchi, C., Nakai, N., et al. 2000, *Proc. SPIE*, 4015, 237
- Tokuyama, S., Oka, T., Takekawa, S., et al. 2019, *PASJ*, 71, S19
- Torii, K., Kudo, N., Fujishita, M., et al. 2010, *PASJ*, 62, 1307
- Torii, K., Fujita, S., Nishimura, A., et al. 2019, *PASJ*, 71, S2
- Umemoto, T., Minamidani, T., Kuno, N., et al. 2017, *PASJ*, 69,

78

- VERA Collaboration, Hirota, T., Nagayama, T., et al. 2020, *PASJ*, 72, 50
- Yamaguchi, C., Sunada, K., Iizuka, Y., et al. 2000, *Proc. SPIE*, 4015, 614

Appendix. Velocity channel maps of the contaminated velocity range

We present the ^{12}CO and ^{13}CO velocity channel maps contaminated by foreground disk components in Figures 7 and 8, respectively. In this velocity range, the CMZ and foreground disk gas components coexist in the same data pixel.

Appendix. Scatter plots and $X_{\text{CO,iso}}$ maps on the LVDs.

We show scatter plots of spectral column densities and $X_{\text{CO,iso}}$ maps on the LVDs from $b = +0.^\circ30$ to $b = -0.^\circ30$ in Figures 9 - 14.

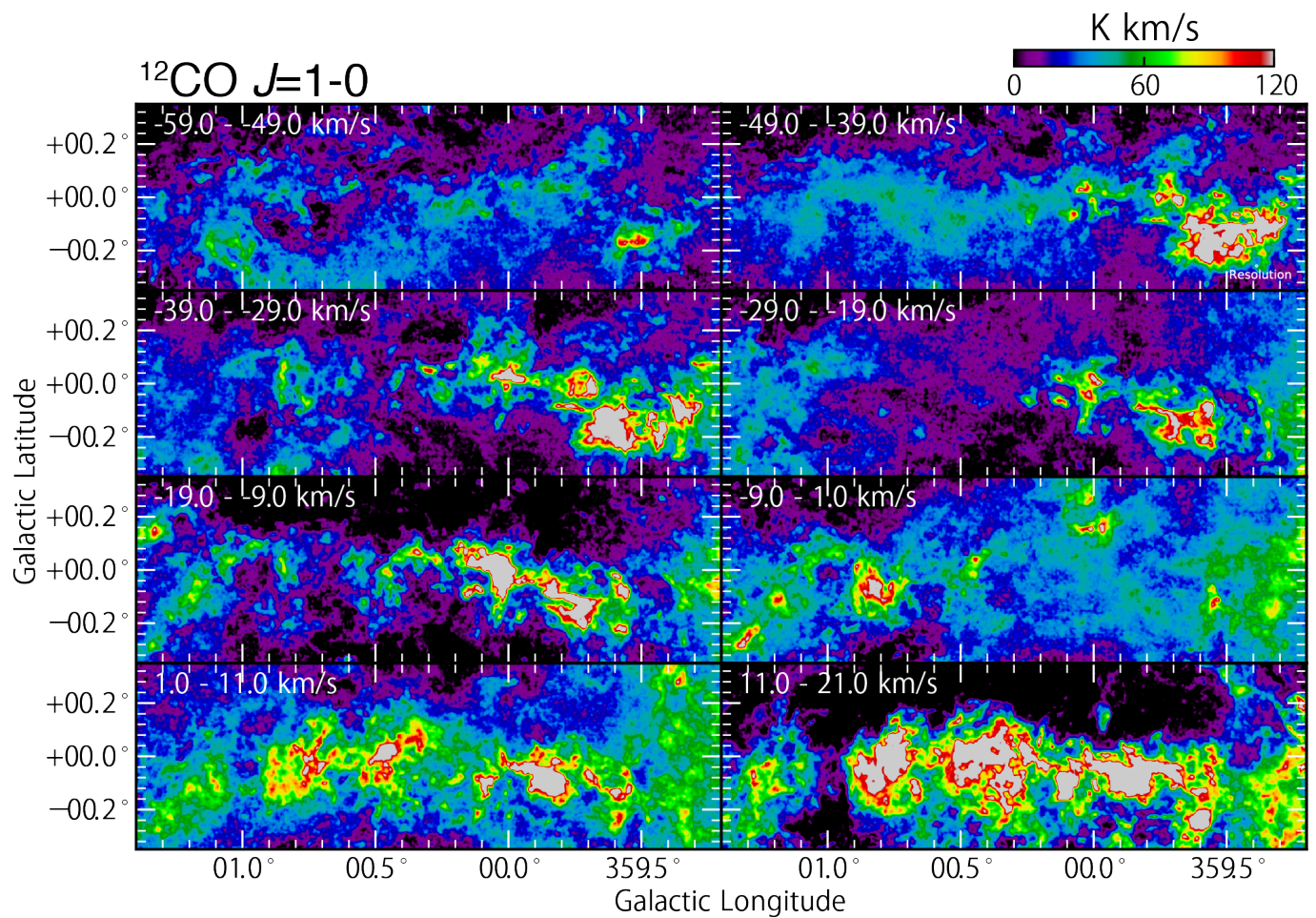


Fig. 7. The $^{12}\text{CO } J=1-0$ channel map of the contaminated velocity range with the CMZ and foreground disk components.

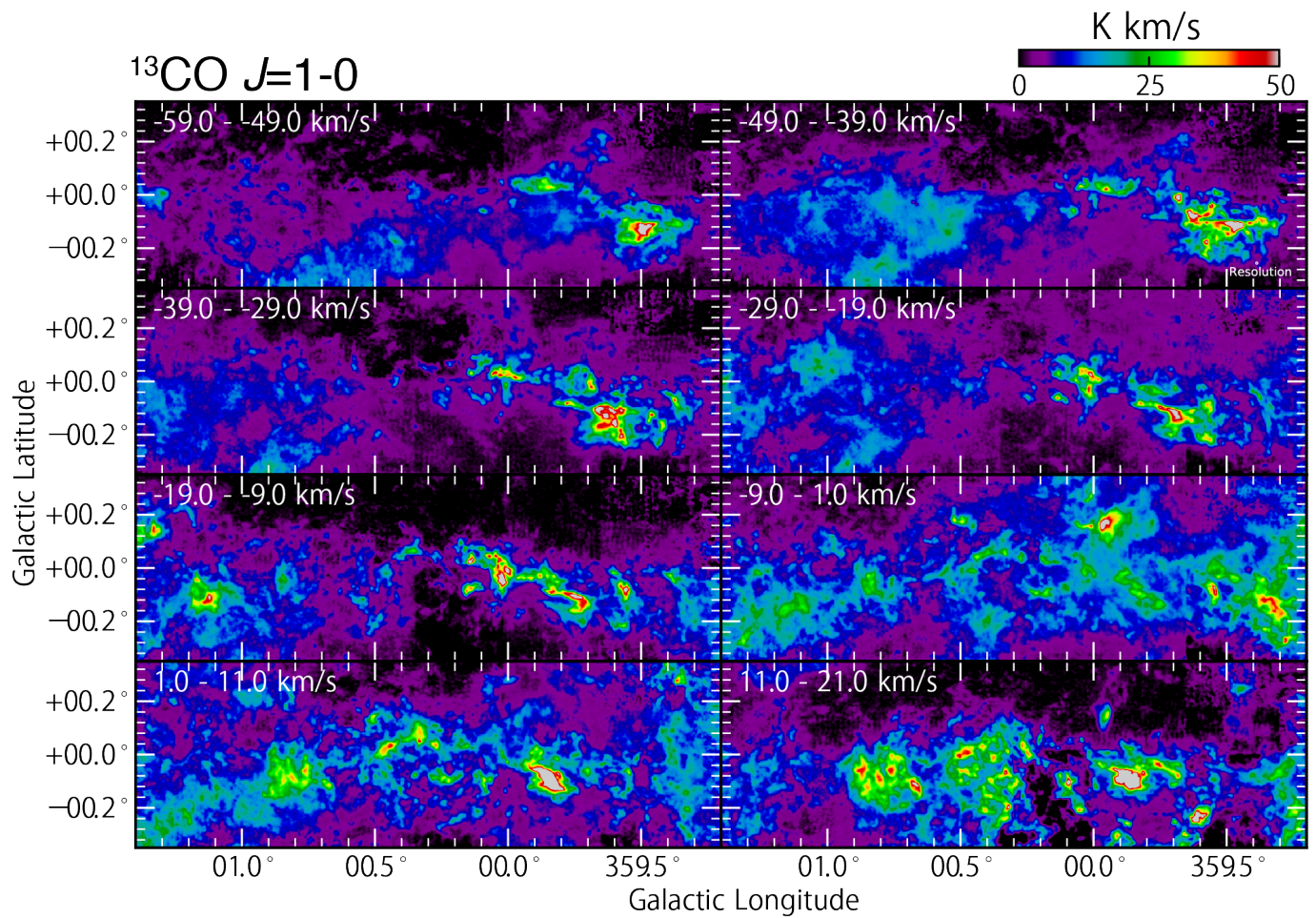


Fig. 8. Same as Figure 7, but for $^{13}\text{CO } J=1-0$.

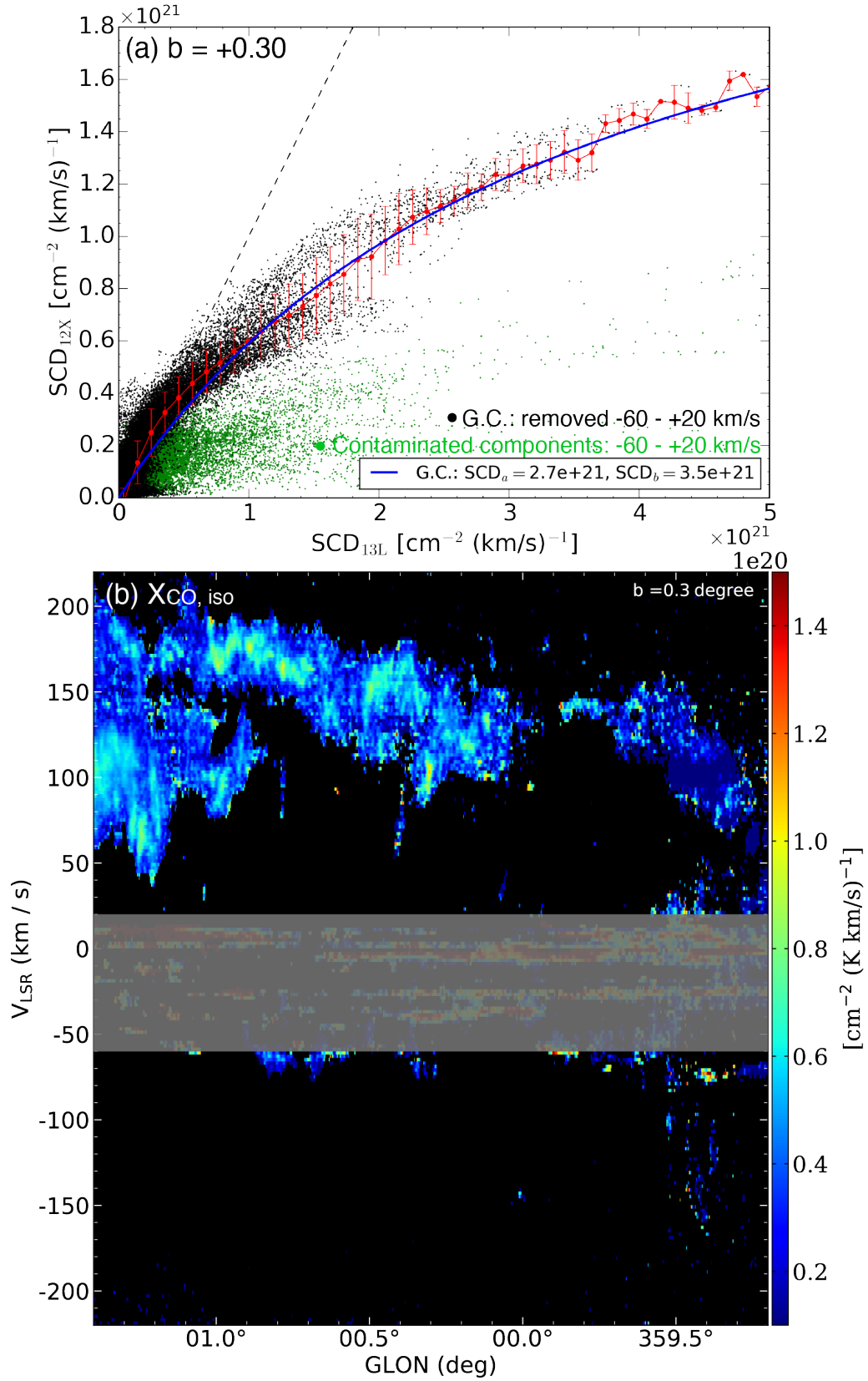


Fig. 9. (a) Same as Figure 4, but for $b = +0.^\circ 30$ (b) Same as Figure 5, but for $b = +0.^\circ 30$

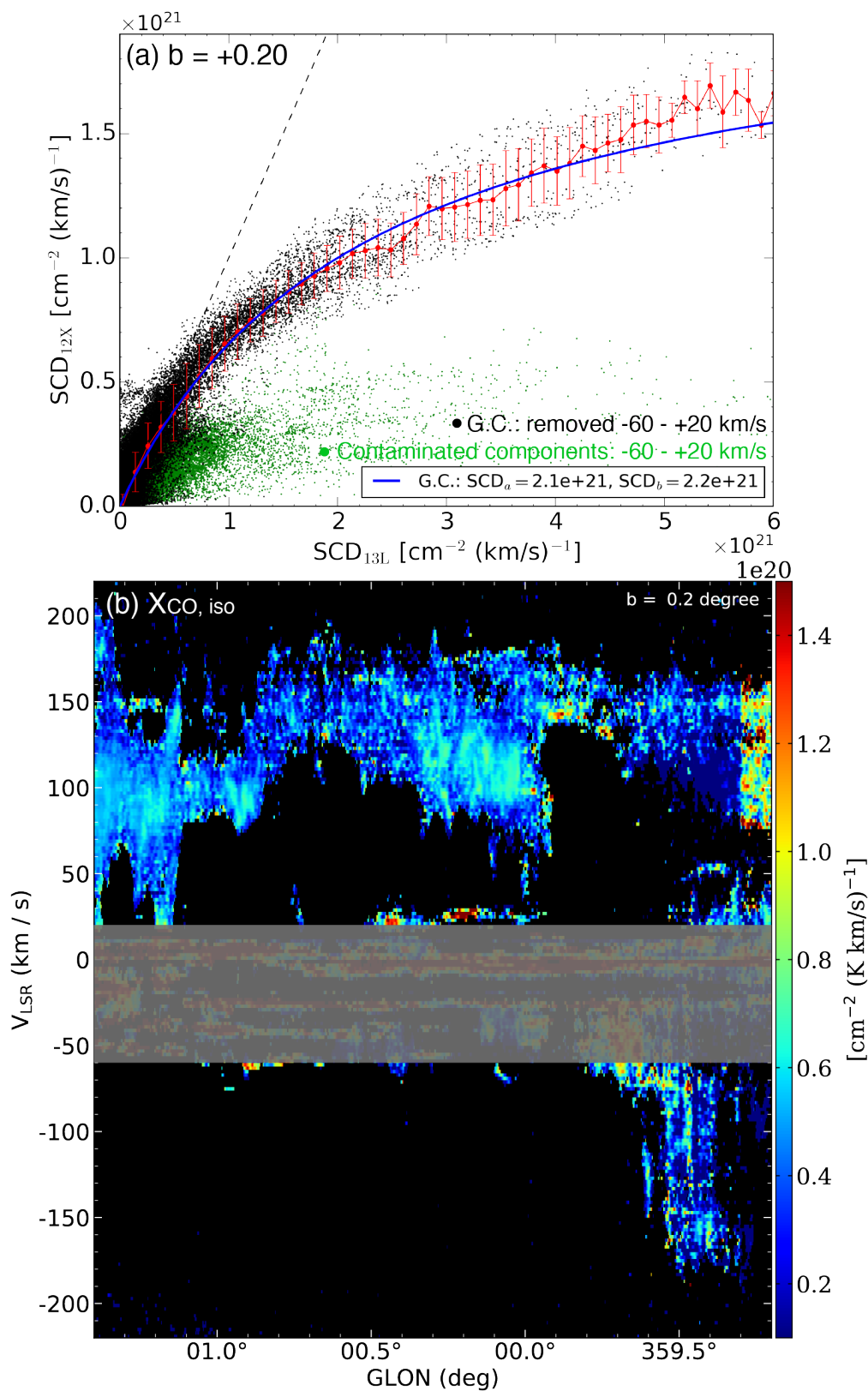


Fig. 10. (a) Same as Figure 4, but for $b = +0.20$ (b) Same as Figure 5, but for $b = +0.20$

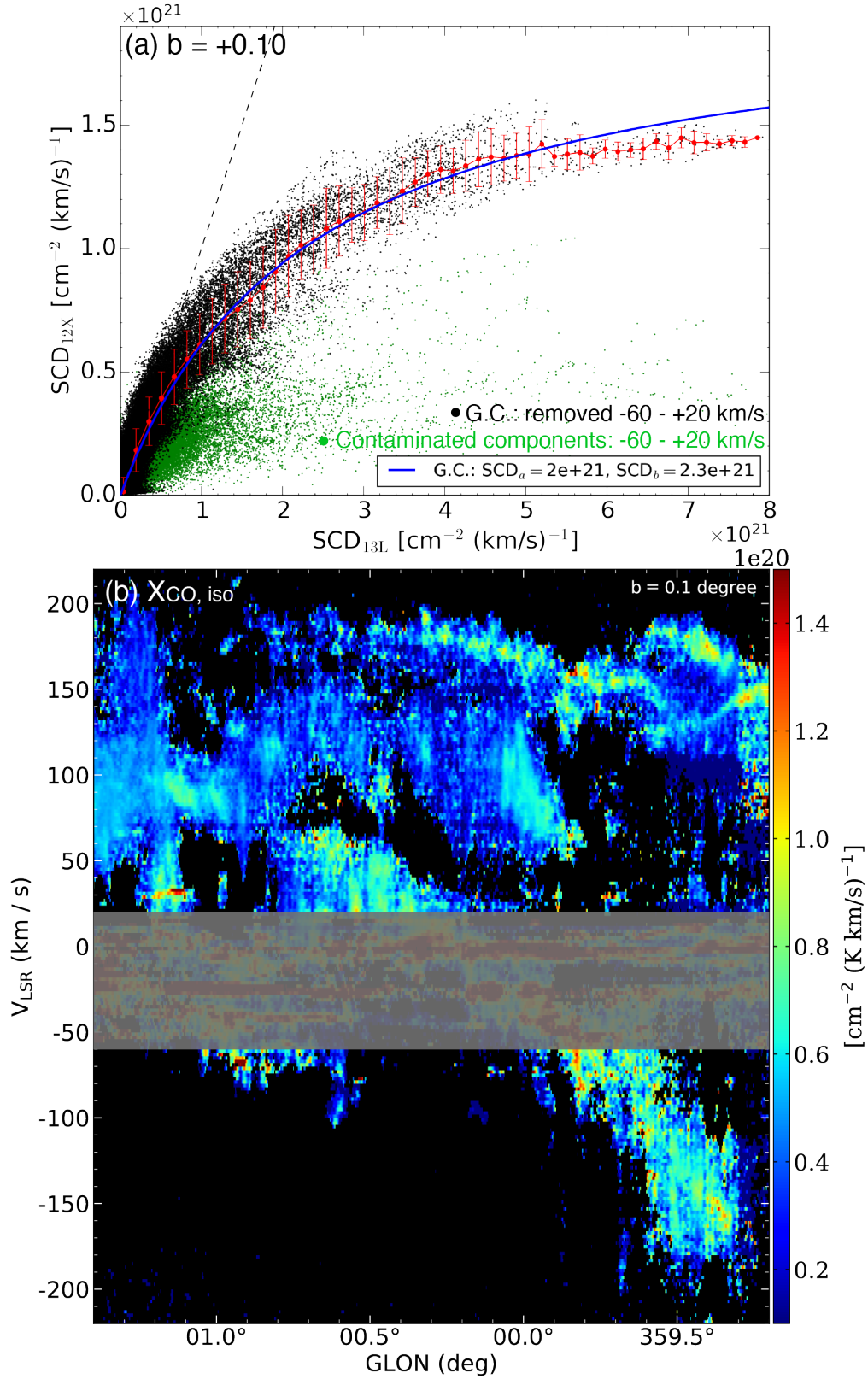


Fig. 11. (a) Same as Figure 4, but for $b = +0.10$ (b) Same as Figure 5, but for $b = +0.10$

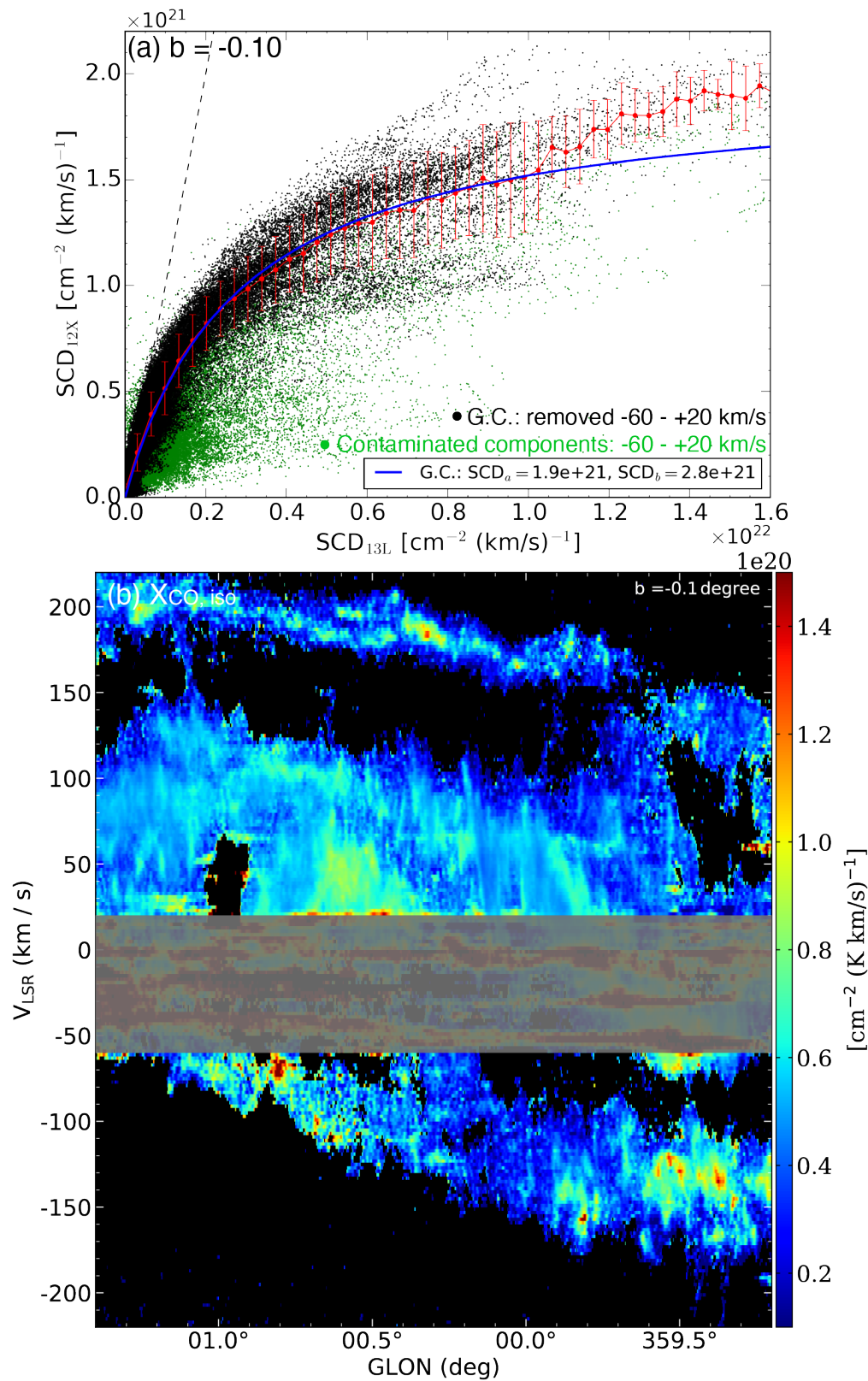


Fig. 12. (a) Same as Figure 4, but for $b = -0.10$ (b) Same as Figure 5, but for $b = -0.10$

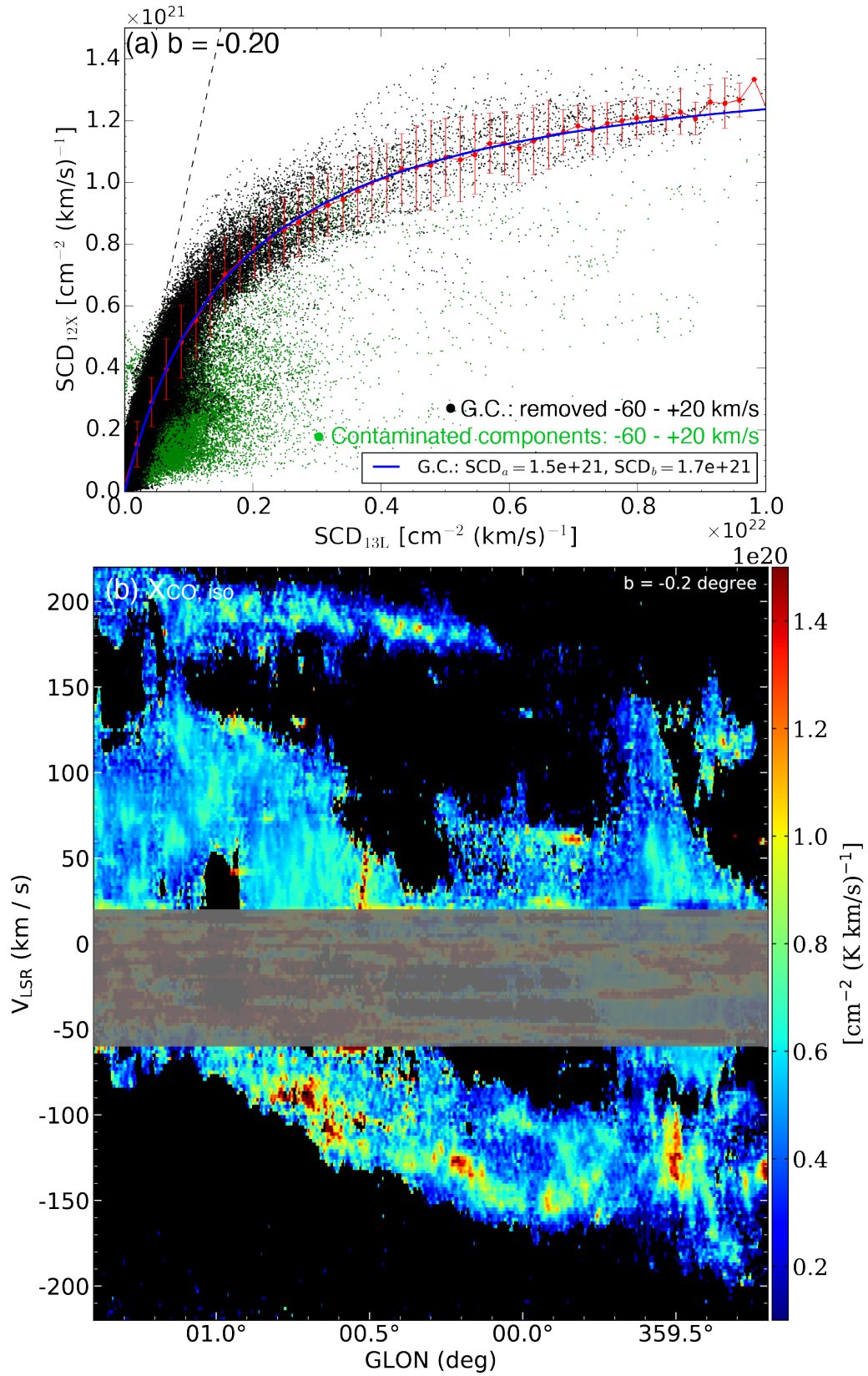


Fig. 13. (a) Same as Figure 4, but for $b = -0.20$ (b) Same as Figure 5, but for $b = -0.20$

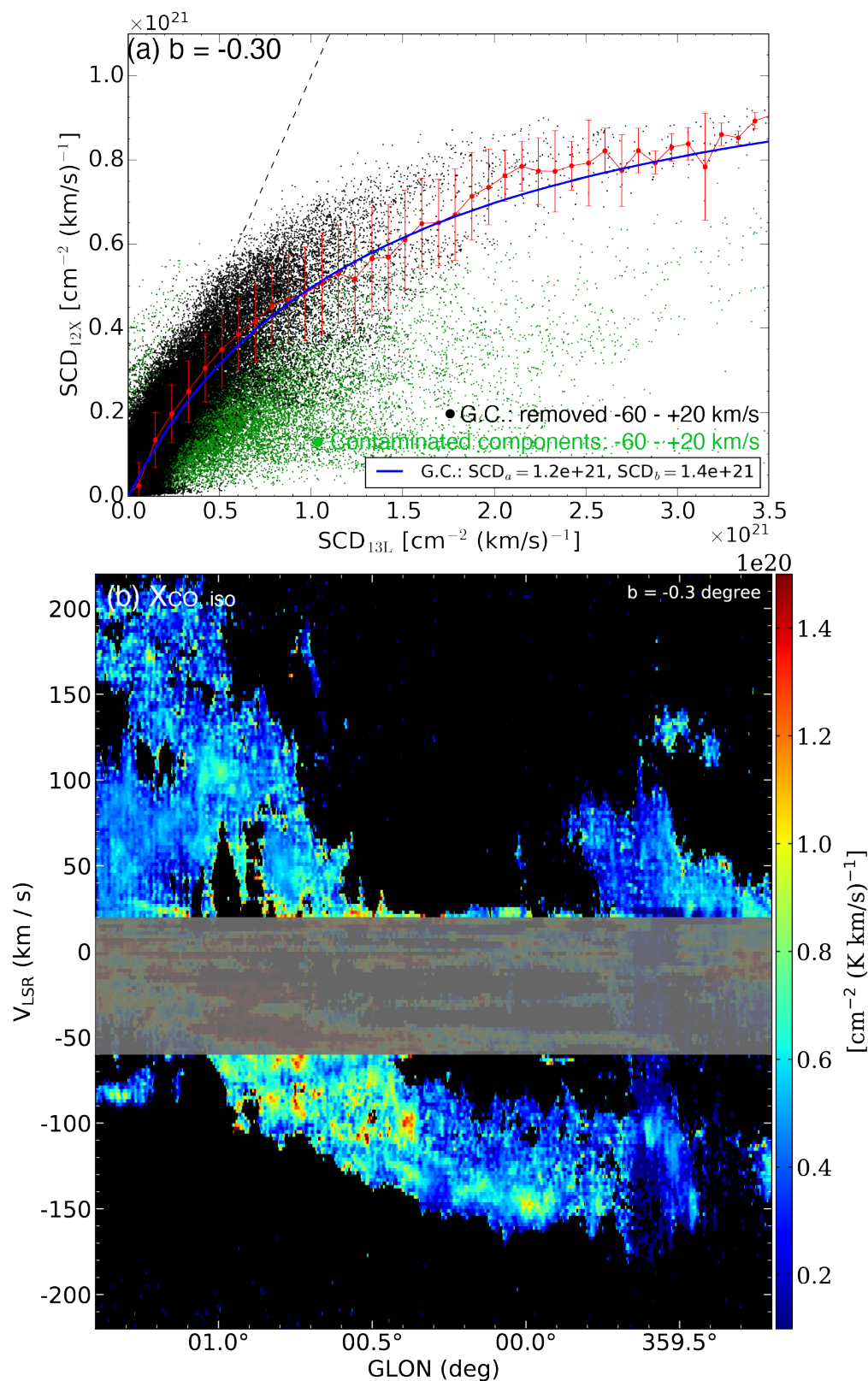


Fig. 14. (a) Same as Figure 4, but for $b = -0.30$ (b) Same as Figure 5, but for $b = -0.30$